Solid Earth Discuss., 6, 1299–1333, 2014
www.solid-earth-discuss.net/6/1299/2014/
doi:10.5194/sed-6-1299-2014

Solid Earth Discussions
Open Access

Thermal conditions during deformation of partially molten crust from TitaniQ geothermometry: rheological implications for the anatectic domain of the Araçuaí belt, Eastern Brazil

G. C. G. Cavalcante[1,2], A. Vauchez[2], C. Merlet[2], M. Egydio-Silva[1], M. H. Bezerra de Holanda[1], and B. Boyer[2]

[1]Instituto de Geociências, Universidade de São Paulo, Rua do Lago, 562, 05508-080, São Paulo, Brazil
[2]Géosciences Montpellier, Université de Montpellier 2 & CNRS Place E. Bataillon, 34095 Montpellier Cedex 05, France

Received: 2 May 2014 – Accepted: 6 May 2014 – Published: 28 May 2014

Correspondence to: G. C. G. Cavalcante (geanecarol@gmail.com)

Published by Copernicus Publications on behalf of the European Geosciences Union.

Abstract

During the Neoproterozoic orogeny, the middle crust of the Araçuaí belt underwent widespread partial melting. At the regional scale, this anatectic domain is characterized by a progressive rotation of the flow direction from South to North, suggesting a 3-D deformation of the anatectic middle crust. To better constrain whether melt volumes present in the anatectic middle crust of the Araçuaí orogen were large enough to allow a combination of gravity-driven and convergence-driven deformation, we used the titanium-in-quartz geothermometer (TitaniQ) to estimate the crystallization temperatures of quartz grains in the anatectic rocks. When possible, we compared these estimates with thermobarometric estimates from traditional exchange geothermobarometers applied to neighboring migmatitic kinzigites. TitaniQ temperatures range from 750 to 800 °C, suggesting that quartz start crystallizing at a minimum temperatures ≥ 800 °C. These results, combined with the bulk-rock composition of isolated leucosomes allow to estimate a minimum of ∼ 30 % melt in the anatectic leucossomes and a corresponding viscosity of $\sim 10^{9}$–1^{10} Pa s. Such a minimum melt content and low viscosity are in agreement with interconnected melt networks observed in the field. Considering that these characteristics are homogeneous over a wide area, this supports that the strength of the middle crust was severely weaken by extensive partial melting turning it prone to gravity-driven channel flow and lateral extrusion.

1 Introduction

Geophysical profiles and geological observations in hot orogens suggest that large volumes of the middle to lower crust have been partially molten during deformation (e.g., Chen et al., 1996; McNamara et al., 1996; Nelson et al., 1996; Alsdorf et al., 1998; Unsworth et al., 2005). Indeed, the presence of even a small fraction of melt may dramatically reduce the strength of rocks and infer on their tectonic behavior (e.g., Rosenberg and Handy, 2005; Labrousse et al., 2011). When partial melting is widespread, it

SED
6, 1299–1333, 2014

may results in the development of a thick, low-strength layer in the crust that deeply alters its rheological behavior during orogeny. In this case numerical models (e.g., Beaumont et al., 2004) suggest that provided the viscosity of the lower to middle crust is low enough (e.g., $\leq 10^{19}$ Pa s), complex deformation such as channel flow may occur in response to combination of tectonic and gravitational forces.

The Araçuaí belt of eastern Brazil is one of several Neoproterozoic belts that involve a large anatectic domain (Oliveira et al., 2000; Vauchez et al., 2007; Petitgirard et al., 2009; Mondou et al., 2012). Most previous studies of the Araçuaí belt, including those studying the anatectic domain, placed emphasis on the characterization of magmatic episodes and strain distribution (e.g., Pedrosa-Soares et al. 2006; Vauchez et al., 2007; Mondou et al., 2012; Cavalcante et al. 2013); only few data on the thermal conditions and partial melting during deformation are available. Preliminary pressure (P) and temperature (T) estimates in mylonites from western part of the belt (e.g., Petitgirard et al. 2009) suggest high-temperature ($\sim 750\,^{\circ}$C), low-pressure (~ 600 MPa) synkinematic conditions.

We have shown recently (Cavalcante et al., 2013) that the anatectic domain in the eastern Araçuaí belt displays a complex 3-D strain distribution that we tentatively interpreted as resulting from the deformation of low-stiffness anatectic middle-crust in response to a combination of tectonic forces from the South America–Africa collision and gravity-driven flow. However, temperature estimates from the anatectic domain are lacking, and such an interpretation assumes that rheological critical conditions that allowed the development of gravity-driven flow in the anatectic middle to lower crust were reached during orogeny. It is, however, difficult to evaluate, even roughly, the synkinematic viscosity of most anatectic domains without estimating equilibrium temperatures and evaluating the melt proportion present in the anatectic rocks during deformation.

Estimates of temperatures were performed using the titanium-in-quartz (TitaniQ) geothermometer developed by Wark and Watson (2006), on migmatitic rocks of the anatectic domain. We have chosen this geothermometer because it requires analysis of only one phase, quartz, its high potential to record temperatures in a major rock

SED
6, 1299–1333, 2014

forming mineral (e.g., Negrini et al., 2014) and because anatexites often do not display adequate mineralogical assemblage required for exchange geothermometers. Furthermore, microstructural observations and microprobe analysis of minerals in anatexites, migmatitic granulite and kinzigites indicate that quartz crystallized in equilibrium with rutile and therefore represents a natural case similar to laboratory experiments performed for the calibration of the TitaniQ geothermometer. To test the reliability of the approach, migmatitic kinzigites with suitable mineralogical assemblages, that bound the anatexites eastward, were analyzed with both conventional thermobarometry and TitaniQ thermometry.

Finally, to better assess the probability of a contribution of gravity-driven flow to the overall deformation, the temperatures estimates and bulk rock composition of anatectic magma were used to evaluate the degree of partial melting of the anatectic middle crust during deformation. This evaluation, combined with field and microstructural observations, allowed us to more reliably constrain the viscosities of the anatectic crust.

2 Geological setting

The convergence between South American and African continents amalgamated rocks of different compositions and ages and formed the Ribeira-Araçuaí-West Congo orogen (e.g., Trompette, 1994; Fig. 1). The Araçuaí belt and its southward continuation, the Ribeira belt, were formed by Neoproterozoic convergence between São Francisco and Congo cratons. The Araçuaí belt is characterized by dominant thrusting of high temperature metamorphic allochthonous units on the São Francisco craton and subordinate orogen-parallel transcurrent motions, whereas the Ribeira belt is characterized by dominant orogen-parallel dextral transcurrent shearing combined with thrusting normal to the belt (Trompette, 1994; Egydio-Silva et al., 2002; Schmitt et al., 2004).

Schematically, the Araçuaí belt is divided into three lithological domains (Oliveira et al. 2000; Vauchez et al. 2007): the western mylonitic unit, the central plutonic unit and eastern anatectic unit (Fig. 2a). The mylonitic domain is composed of high temperature

SED
6, 1299–1333, 2014

metasedimantary mylonites injected by large volume of leucogranite sills. These rocks were thrust westward onto the para-autochthonous metasediments of the São Francisco craton (Petitgirard et al., 2009). Eastward, the central plutonic domain comprises tonalite and granodiorite bodies deformed in the magmatic state (Mondou et al., 2012). The eastern anatectic domain is dominated by a variety of anatexites and anatectic granites that result from pervasive partial melting of metasedimentary rocks under crustal P, T conditions (Vauchez et al., 2007). This anatectic domain is ~ 300 km long and 50–100 km wide. Migmatitic granulite forms rafts embedded into the anatexites. Migmatitic kinzigites occur to the southeast of the anatexites; they progressively grade westward to diatexites and leucogranites, suggesting a transition from kinzigites to anatexites. Structural mapping in the anatectic unit using the Anisotropy of Magnetic Susceptibility (AMS) highlighted a complex pattern of lineation the trend of which rotate from WSW–ENE in the southern part of the study area to NW–SE in the northern part and to N–S in the easternmost part (Cavalcante et al., 2013; Fig. 2b). Considering the progressive transition between the various dominant orientations of lineation together with evidence supporting that, independently of the flow direction, the fabric formed in the magmatic state, led us to suggest that the complex deformation of the anatexites result from a single, probably, protracted tectonic event.

Thermochronological data from the mylonitic domain suggest that this region remained hot (750 to > 600 °C) for tens of million years (580–530 Ma) due to a low cooling rate ($\leq 5\,^{\circ}\mathrm{C\,My^{-1}}$; Petitgirard et al., 2009). Conventional thermobarometric estimates performed by Munhá et al. (2005) in the migmatitic gneisses from the southern part of the Araçuaí belt suggest that metamorphic peak and partial melting took place at temperatures of 820 °C ± 30 °C and at pressures of 650 MPa ± 50 MPa.

3 Samples: location and description

Six samples were selected from the anatectic unit (Fig. 2a). Three samples come from the anatexites (Ar1258, Ar1299 and Ar1326), one from the migmatitic granulite of the

SED
6, 1299–1333, 2014

northern domain (Ar1296), and two from the migmatitic kinzigites of the southeastern domain (Ar949 and Ar1083). At the outcrop scale the anatexites display a clear magmatic foliation marked by the preferred alignment of biotite and feldspar grains (Fig. 3a). In situ leucosomes are frequently observed in metatexites that preserve a gneissic banding (Fig. 4). Migmatitic features such as stromatic, nebulitic and schlieren leucosomes, rich in garnet and feldspar, are also common (Fig. 3b and c).

The migmatitic kinzigites display a gneissic banding characterized by alternating felsic and mafic layers. Stromatic and coarser-grained leucosomes, rich in feldspar, garnet and quartz, are embedded parallel to banding (Fig. 3d and e).

The migmatitic granulite is mafic in composition and does not show a clear macroscopic fabric. It does, however, contain narrow strings of leucosomes pointing to limited partial melting (Fig. 3f).

3.1 Petrographic observations

Anatexites and kinzigites are composed of K-feldspar, quartz, plagioclase, biotite, garnet, cordierite, sillimanite, ilmenite and rutile. The migmatitic granulite also contains orthopyroxene ± magnetite.

Quartz usually displays interstitial shapes (Fig. 5a), although this is less frequent in the migmatitic granulite that contains less quartz. It has irregular grain boundaries, with sizes ranging from ~ 200 µm to ~ 0.2 cm, and is mostly free of substructure, with exception of an undulose extinction or faint subgrain boundaries (Fig. 5b).

Plagioclase reaches ~ 0.4 cm in size and dominantly displays subeuhedral shapes; in many cases, it is surrounded by interstitial films of quartz along grain boundaries (Fig. 5c). In the migmatitic granulites, many crystals of plagioclase display deformation twins attesting to the high temperature deformation (Fig. 5d).

K-feldspar is ~ 0.3 cm in size and displays curved, lobate and straight grain boundaries. It often exhibits myrmekites and is free of evidence of intracrystalline deformation.

SED
6, 1299–1333, 2014

Biotite displays a strong preferred orientation (Fig. 5a and e). It is euhedral, subeuhedral and acicular in shapes, with straight to curved grain boundaries. It tends to arch around large K-feldspars (Fig. 5f). In the migmatitic kinzigites, a few kinked biotites are observed.

Sillimanite is acicular and garnet is rounded, but locally elongate parallel to foliation, with frequent inclusions of quartz, biotite, ilmenite and rutile.

4 TitaniQ temperature estimates

The TitaniQ geothermometer is based on substitution of Si by Ti in quartz. Since the substitution is dependent on temperature (Wark and Watson, 2006), Ti concentration in quartz is correlated to its formation temperature. To develop this geothermometer, Wark and Watson (2006) synthesized quartz in the presence of rutile and aqueous fluid or hydrous silicate melt at temperatures ranging from 600 to 1000 °C and 1.0 GPa of pressure. This geothermometer relates the temperature (T) of crystallization to the Ti content of quartz according to:

$$\mathrm{Log}(\mathrm{Ti}_{\mathrm{quartz}}) = 5.69 - 3765/T \quad (1)$$

where $\mathrm{Ti}_{\mathrm{quartz}}$ is the Ti concentration in quartz in ppm and T is the temperature in Kelvin. No adjustment was necessary for this equation because both rutile and ilmenite were present in the analyzed samples. TitaniQ has already been applied to characterize thermal histories of migmatitic (Storm and Spear, 2009), mylonitic (Kohn and Northrup, 2009; Grujic et al., 2011) and volcanic rocks (e.g., Ehrlich et al., 2012).

4.1 Material and procedure

Microprobe analysis and backscattered electron images were performed on a CAMECA SX-100 electron probe instrument equipped with five wavelength-dispersive X-ray spectrometers. Some of the X-ray spectrometers are equipped with

SED
6, 1299–1333, 2014

a large, high-efficiency Johansson crystal. Before microprobe analysis, the selected samples were imaged by cathodoluminescence and no evidence of zoning was observed (Fig. 6). All quartz grains display an intense homogeneous dark blue color, suggesting that multiple thermal events are unlikely. We have selected large and/or interstitial quartz grains (≥ 0.3 mm) having similar aspects, no inclusion and nor evidence of intracrystalline deformation or microfracture.

Four to five quartz grains from each sample were analyzed. Microprobe analyses were made along transverse profiles with spacing of at least 120 µm (Fig. 7), and preferentially in areas free of rutile and impurities. More than 370 Ti-in-quartz analyses were performed on samples from the anatectic domain.

4.2 Analytical procedures

Accurate characterization of trace elements using the Electron Probe Micro Analysis (EPMA) requires optimal analytical conditions (e.g., Merlet and Bodinier, 1990; Bodinier et al., 1996; Kalfoun et al., 2002b). The choice of the accelerating voltage value is essential because it influences the X-ray emission yield and bias. The best spatial resolution is obtained with a low accelerating voltage, whereas higher voltages are needed for transition and trace elements. These constraints require a compromise between X-ray line, peak counting statistics, background subtraction, electron beam size, beam drift, quantification uncertainty, stray radiation and sample damage. In order to find optimum balance, recent developments in microanalysis, such as spectrum simulation and X-ray emission modeling (Fournier et al., 1999; Kalfoun et al., 2002b), were taken into account.

Traces of titanium in quartz are relatively easy to identify but care must be taken against sample damage and Bremsstrahlung fluorescence ("braking radiation") of Ti atoms in close proximity to rutile (Wark and Watson, 2006), ilmenite and biotite. The Bremsstrahlung effect is a form of secondary fluorescence produced by elastic interaction of the 15 kV incident electrons with the quartz lattice (e.g., Bastin et al., 1984) that can be calculated by Monte Carlo simulation. At 20 kV accelerating voltage, a minimum

SED
6, 1299–1333, 2014

gap of 200 microns between these minerals is required in order to avoid erroneously estimates of Ti concentration.

Concentrations were measured using an accelerating voltage of 20 kV, a beam current of 200 nA and a 50-micron defocused probe to reduce irradiation damage. Electron beam current was selected to compromise between a high X-ray counting rate and minimal sample damage. The Ti concentration was determined by simultaneously counting Ti K-alpha X-ray lines using three spectrometers with large pentaerythritol (LPET) crystals in a Johansson configuration and averaging the results.

Bremsstrahlung background was subtracted using a method that combines the measured and calculated background spectra from samples for which neither spectral lines nor absorption edges were observed in the region of interest (Kalfoun et al., 2002b). The peak and background acquisition time for each point for all elements and all five spectrometers was 480 s. The counting time of 480 s is the maximum time that a defocused beam of 50 microns can shine on a sample without damaging it significantly. The corresponding integration time and beam current provide a typical statistical error (peak counting) of approximately 1.5 % for a 100 ppm Ti concentration and thus a 7 ppm limit of detection. Concentrations are obtained from raw intensities by using the "X-PHI" quantification procedure (Merlet, 1994). Natural SiO_2 and TiO_2 are used as standards for Si and Ti, respectively.

The global uncertainty of Ti concentration at a single point, obtained by adding the random and systematic uncertainties in quadrature, is ±6 % (2σ) at ≥ 100 ppm; these estimates consider errors from peak counting (1.5 %), background estimates (2 %), sample damage and contamination (1.5 %) and uncertainties in standard composition and quantification procedure (1 %).

4.3 Results

The Ti content in quartz from anatexites, migmatitic kinzigites and granulite, and the calculated temperatures are presented in Table 1 and Fig. 8. A temperature was calculated from each analytical spot. The average Ti content is ~ 129 ppm in anatexites,

SED
6, 1299–1333, 2014

~ 142 ppm in migmatitic kinzigites and ~ 112 ppm in migmatitic granulite. Average crystallization temperatures calculated for all quartz grains from the samples of the anatectic domain ranges between 700 and 810 °C. Single quartz crystals display a rather homogenous distribution of titanium, consequently a uniform temperature values (Fig. 8). Specimen Ar1296, a mafic granulite, constitute an exception with temperature averages calculated for five quartz crystals spanning from 710 to 785 °C with a mean temperature of 755 ± 16 °C. This rock is derived from a mafic magmatic protolith in which the presence of a rather small amount of interstitial quartz and large amount of plagioclase locally showing mechanical twins (Fig. 5d) suggests limited partial melting during high temperature, solid-state deformation.

For the anatexites, calculated temperature averages of 747 °C ± 15 °C and 780 ± 16 °C are determined for samples Ar1258 and Ar1299 from the central part of the study area and 792 °C ± 17 °C for sample Ar1326 from the southeast. For the partially molten kinzigites (samples Ar949 and Ar1083) high temperature averages are observed, 787 °C ± 17 °C and 794 °C ± 17 °C, respectively.

5 Exchange reaction thermobarometry

Thermobarometric estimates using traditional exchange reactions were determined from the migmatitic kinzigites (samples Ar949, Ar1083 and Ar1076) for comparison with the temperatures determined with the TitaniQ thermometry. Sample Ar1076 collected close to site Ar1083 was not analyzed for TitaniQ thermometry, but used for exchange thermobarometry due to an adequate mineral assemblage.

Temperatures were obtained using the geothermometer developed by Ferry and Spear (1978), Bhattacharya et al. (1991), and Bhattacharya et al. (1988). Pressures were estimated using the garnet-plagioclase-biotite-quartz (GPBQ) geobarometer (Wu et al., 2004). We chose these geothermobarometers by considering the textural characteristics of the analyzed mineral pairs, i.e. those displaying equilibrium relations ex-

SED
6, 1299–1333, 2014

pected on the temperature interval on which the geothermobarometers were calibrated. The resulting *P-T* estimates are presented in Table 2.

Cores and rims of garnet, biotite, plagioclase, cordierite and orthopyroxene were analyzed (Table 3). Garnet-biotite, garnet-orthopyroxene and garnet-cordierite geothermometers and GPBQ geobarometer applied to analyses from the cores of the crystals suggest that the minimum temperatures for peak metamorphic recorded in migmatitic kinzigites range between 720 and 840 °C ± 50 °C and pressure between 650 and 700 MPa ± 100 MPa. These temperatures are very close to those obtained with TitaniQ (794 °C ± 17 °C and 787 °C ± 17 °C) for the same samples. Significantly lower temperatures (550 to 780 °C) obtained in garnet, biotite and opx rims likely represent cooling during retrogressive metamorphic conditions. However, more data are required to better constrain the significance of these values.

6 Discussion

Paleotemperatures recorded by the anatectic rocks of the eastern part of the Araçuaí belt have been calculated from Ti content in quartz. Individual crystals display rather homogeneous compositions (Fig. 7) suggesting that Ti diffusion after crystallization was limited. For instance analysis from sample AR949 show a good correlation between temperatures estimated from Ti-in-quartz and those estimated from garnet and biotite core compositions (Tables 1 and 2). Garnet and biotite rim compositions however have recorded cooling to significantly lower temperatures, which was not recorded by Ti-in-quartz. This suggests that post-crystallization cooling had little effect on the Ti content in quartz.

Temperatures obtained from the studied samples range from 700 to 810 °C with individual average values between 750 and 800 °C Fig (Fig. 8). For each sample, the analyzed grains define a temperature range that likely represents the minimum temperature interval over which quartz crystallized from the magma during cooling and solidification of the anatectic domain. Data lying significantly outside this domain of

SED
6, 1299–1333, 2014

temperatures and contrasting strongly with the temperature of neighboring points of analysis may be regarded as out of equilibrium and thus have not further been taken into account. The upper limit of this temperature interval is considered as representing the initial stage of interstitial quartz crystallization, and consequently the minimum value for the peak temperature to which the anatectic domain was submitted. Samples Ar949, Ar1083, Ar1299 and Ar1326 strongly suggest a minimum temperature ~ 800 °C or slightly above. Samples Ar1258 and Ar1296 suggest a slightly lower temperature in the range 750–800 °C.

Migmatites and silicate melts containing Al-rich minerals are usually generated by partial melting of metasedimentary rocks in the crust at minimum temperatures ≥ 700 °C (e.g., MacRae and Nesbit, 1980; White et al., 2003). Viscosity of resulting melts has been estimated at ~ $10^{4.5}$ Pa s (Scaillet et al., 1998) or 10^{3} to 10^{6} Pa s (Clemens and Petford, 1999). The viscosity of solid rocks differs from the viscosity of their melts by several orders of magnitude. Therefore, the viscosity of partially molten rocks varies widely, depending on the melt fraction, the viscosities of the molten and crystalline fractions, and on the shape and spatial distribution of solid particles (e.g., Arzi, 1978). Experiments suggest that the effect of the melt fraction on the viscosity of migmatite dominates the effects of temperature, pressure and stress, which vary less abruptly (Arzi, 1978; Rosenberg and Handy, 2005). According to Arzi (1978), a rock containing a melt fraction of 20 % ± 10 % would reach the critical melt percentage (RCMP), above which, due to the connectivity of the melt fraction its viscosity would decrease and rapidly approximate the melt's viscosity. In their compilation of experiments, Rosenberg and Handy (2005) suggest that departure from the solid behavior may become significant for melt fractions as low as 7 %.

The amount of titanium preserved in quartz is in equilibrium with the temperature prevailing when quartz crystallized from the melt. The peak temperature reached by the anatexites was therefore higher than the temperatures calculated using the TitaniQ calibration (750–800 °C). *P-T* estimates from exchange geothermobarometers suggest that the minimum temperatures and pressures for peak metamorphic condi-

SED
6, 1299–1333, 2014

tions recorded in samples of migmatitic kinzigites from which derive, at least partly, the anatexites are at ~ 800 °C ± 50 °C and ~ 650–700 MPa ± 100 MPa. They are also consistent with estimates from Munhá et al. (2005; ~ 820 °C, 650 MPa). A temperature of 800 °C for the anatexites seems therefore to be a conservative value to further discuss their rheological characteristics.

We have estimated the solid/liquid proportion in the leucosome of the anatexites using the rhyolite-MELTS software (Gualda et al., 2012) for temperature and pressure in the range 800–850 °C and 600–700 MPa, H_2O content 1–2 %, and bulk rock composition of 7 samples of leucosome (Table 4). The proportion of liquid in the system, inferred using these parameters, is systematically larger than 28 % and may reach up to ~ 50 %. The viscosity of the liquid phase varies in the range 10^5–10^6 Pa s. MELTS predicts progressive crystallization of quartz (in proportion inversely proportional to the amount of liquid in the system) with decreasing temperature. Such values are in agreement with the ubiquitous presence of interstitial quartz and films of quartz or feldspar separating inherited crystals, and also with the stromatic, schollen and locally nebulitic aspect of the anatexites (e.g., Sawyer, 2008). We may therefore consider that at 800 °C and 650 MPa, 30 % liquid present in the leucosome is a reasonable value that may be used to evaluate the viscosity of the suspension. For such proportion of solid in the magma (70 %), MELTS does not compute the viscosity of the system. We therefore roughly estimated this viscosity using the Roscoe (1952) equation:

$$\eta_e = \eta(1 - 1.35\varphi)^{-2.5}$$

where η_e is the effective viscosity of a suspension made of a liquid of viscosity η, and φ is the solid fraction of spherical particles. Computed viscosity of the suspension varies between ~ 10^8 and ~ 10^{10} Pa s for 30 % of liquid phase with a viscosity of 10^5 and 10^6 Pa s. If a rather large diversity of size is taken into account, the viscosity of the suspension decrease of about one order of magnitude (e.g., Kansal et al., 2002).

Restitic bodies in the anatectic domain of the Araçuaí belt, independently of their size (cm to km), are systematically immersed in leucosome or anatectic granites that

SED
6, 1299–1333, 2014

forms a network of magma (Fig. 4) connected at the regional scale. This supports that the viscosity of the partially molten crust was closer to the magma viscosity than to the solid-rock viscosity (e.g., Sawyer, 2008) and, in any case, much lower than the viscosity of 10^{19} Pa s, below which Beaumont et al. (2004) numerical models for the Himalayan orogen predict an increasing probability of large-scale horizontal channel flow being triggered in response to gravity forces.

The anatectic crust of the Araçuaí belt was formed during the east-west convergence between the South American and African plates. Seismic receiver functions suggest that the current crustal thickness of the Araçuaí-Ribeira belt is ~ 32–41 km (Assumpção et al., 2013). Considering the pressure estimates obtained in this study for the minimum conditions for metamorphic peak of the migmatitic kinzigites (650–700 MPa), we can infer that approximately 25 km of the continental crust have been removed. It follows that the crust thickness reached at least 60 km during the continent-continent collision. Such a thick crust, an abnormally high geotherm ($\geq 30\,^{\circ}\mathrm{C\,km^{-1}}$) and a slow cooling rate ($\leq 5\,^{\circ}\mathrm{C\,My^{-1}}$; Petitgirad et al., 2009) resulted in widespread partial melting of the middle to lower crust, which dropped the viscosity of the anatectic layer to values low enough ($\ll 10^{19}$ Pa s) for enabling a gravity-induced component of deformation. Considering the cooling rate, the large volume of melt produced during orogeny and the latent heat of crystallization release by this anatectic layer, we can hypothesize that this low-viscosity layer remained so over a very long period (tens of My), its viscosity increasing slowly with the decrease in temperature. This supports that the gravity-driven deformation may have combined with deformation due to east-west convergence between the South America and Africa proto-continents, resulting in a complex, 3-D flow of the anatectic middle crust.

7 Conclusions

Temperature estimates from the middle crust of the Araçuaí belt acquired using the titanium-in-quartz geothermometer in anatectic rocks are similar to those obtained from

SED
6, 1299–1333, 2014

exchange geothermometry in neighboring kinzigites that have mineral assemblages suitable for such analysis. This good agreement supports that the TitaniQ geothermometer provides reliable crystallization temperatures of quartz in anatectic rocks. These estimates point to minimum temperature and pressure conditions for metamorphic peak above 800 °C and 650 to 700 MPa. Solid/liquid fractions computed using conservative P and T values and the chemical compositions of several anatexites suggest that at least 30 % of melt was present during orogeny, a proportion consistent with the presence of in situ leucosomes and stromatic, nebulitic and schlieren structures in the anatexites. Such a proportion of melt is large enough to promote melt interconnectivity, as mentioned by Arzy (1978) and Rosenberg and Handy (2005) for instance. Rough estimates suggest that the partially molten middle crust had a viscosity significantly lower than the 10^{19} Pa s, which is suggested by Beaumont et al. (2004) as the upper limit bellow which a rheologically weak crust is prone to develop channel flow during orogeny. Therefore, considering the size (~ 300 km × 50–100 km) of the anatectic domain of the Araçuaí belt, the large orogenic thickness of the crust, the abnormally high temperature gradient, the low cooling rate and the transient low-viscosity of the partially molten middle crust, the 3-D flow pattern that characterizes the anatectic domain of the Araçuaí belt (e.g., Cavalcante et al., 2013) may result from the deformation of the low-viscosity middle crustal anatectic layer through gravity-driven escape flow associated to convergence-driven shortening.

Acknowledgements. The first author is grateful to the Fundação de Amparo à Pesquisa do Estado de São Paulo (FAPESP, Brazil)-Project 2010/03537-7 and to the Coordenação de Aperfeiçoamento Pessoal de Nível Superior (CAPES, Brazil)-Project 419011-4 for the granting of Ph.D. scholarships. We are indebted to Jean-Luc Bouchez and Loïc Labrousse for their criticisms that helped to substantially improve this manuscript. Additional assistance by Bénédicte Cenki-Tok, Lucelene Martins and Fleurice Parat is greatly appreciated.

SED
6, 1299–1333, 2014

References

Alsdorf, D., Makovsky, Y., Zhao, W., Brown, L. D., Nelson, K. D., Klemperer, S., Hauck, M., Ross, A., Cogan, M., Clark, M., Che, J., and Kuo, J.: INDEPTH (International Deep Profiling of Tibet and the Himalaya) multichannel seismic reflection data; description and availability, J. Geophys. Res., 103, 26993–26999, 1998.

Arzi, A.: Critical phenomena in the rheology of partially melted rocks, Tectonophysics, 44, 173–184, 1978.

Assumpção, M., Bianchi, M., Julià, J., Dias, F. L., França, G. S., Nascimento, R., Drouet, S., Pavão, C. G., and Albuquerque, D. F.: Crustal thickeness map of Brazil: data compilation and main feautures, J. S. Am. Earth Sci., 43, 74–85, 2013.

Bastin, G. F., Loo, F. J. J., Vosters, P. J. C., and Vrolijk, J. W. G. A.: An iterative procedure for the correction of secondary fluorescence effects in eléctron probe microanalysis near phase boundaries, Spectrochim. Acta, 39, 1517–1522, 1984.

Beaumont, C., Jamieson, R. A., Nguyen, M. H., and Medvedev, S.: Crustal channel flows: 1. Numerical models with applications to the tectonics of the Himalayan-Tibetan orogen, J. Geophys. Res., 109, 1–29, 2004.

Bhattacharya, A., Mazumdar, A. C., and Sen, S. K.: Fe-Mg mixing in cordierite: constraints from natural data and implications for cordierite-garnet geothermometry in granulites, Am. Mineral., 73, 338–344, 1988.

Bhattacharya, A., Krishnakumar, K. R., Raith, M., and Sen, S. K.: An improved set of a – X parameters for Fe–Mg–Ca garnets and refinements of the orthopyroxene–garnet thermometer and the orthopyroxene–garnet–plagioclase–quartz barometer, J. Petrology, 32, 629–656, 1991.

Bodinier, J.-L., Merlet, C., Bedini, R. M., Simien, F., Remaidi, M., and Garrido, C. J.: Distribution of Nb, Ta and other highly incompatible trace elements in the lithospheric mantle: the spinel paradox, Geochim. Cosmochim. Ac., 60, 545–550, 1996.

Cavalcante, G. C. G., Egydio-Silva, M., Vauchez, A., Camps, P., and Oliveira, E.: Strain distribution across a partially molten middle crust: insights from the AMS mapping of the Carlos Chagas Anatexite, Araçuaí belt (East Brazil), J. Struct. Geol., 55, 79–100, 2013.

Chen, L., Booker, J. R., Jones, A. G., Wu, N., Unsworth, M. J., Wei, W., and Tan, H.: Electrically conductive crust in southern Tibet from INDEPTH magnetotelluric surveying, Science, 274, 1694–1696, 1996.

SED
6, 1299–1333, 2014

Clemens, J. D. and Petford, N.: Granitic melt viscosity and silicic magma dynamics in contrasting tectonic settings, J. Geol. Soc. Lond., 156, 1057–1060, 1999.
Egydio-Silva, M., Vauchez, A., Bascou, J., and Hippertt, J.: High-temperature deformation in the Neoproterozoic transpressional Ribeira belt, southeast Brazil, Tectonophysics, 352, 203–224, 2002.
Ehrlich, K., Vers, E., Kirs, J., and Soesoo, A.: Using a titanium-in-quartz geothermometer for crystallization temperature estimation of the Palaeoproterozoic Suursaari quartz porphyry, Est. J. Earth Sci., 61, 195–204, 2012.
Ferry, J. M. and Spear, F. S.: Experimental calibration of the partitioning of Fe and Mg between biotite and garnet, Contrib. Mineral. Petr., 66, 113–117, 1978.
Fournier, C., Merlet, C., Dugne, O., and Fialin, M.: Standardless semi-quantitative analysis with WDS-EPMA, J. Anal. Atom. Spectrom., 14, 381–386, 1999.
Grujic, D., Stipp, M., and Wooden, J. L.: Thermometry of quartz mylonites: importance of dynamic recrystallization on Ti-in-quartz reequilibration, Geochem. Geophy. Geosy., 12, 1–19, 2011.
Gualda, G. A. R., Ghiorso, M. S., Lemons, R. V., and Carley, T. L.: Rhyolite-MELTS: a modified calibration of MELTS optimized for silica-rich, fluid-bearing magmatic systems, J. Petrol., 25, 1–16, doi:10.1093/petrology/egr080, 2012.
Kalfoun, F., Ionov, D., and Merlet, C.: HFSE residence and Nb-Ta ratios in metasomatised, rutile-bearing mantle peridotites, Earth Planet. Sci. Lett., 199, 49–65, 2002a.
Kalfoun, F., Merlet, C., and Ionov, D.: Determination of Nb, Ta, Zr and Hf in micro-phases at low concentrations by EPMA, Mikrochim. Acta, 139, 83–91, 2002b.
Kansal, A. R., Torquato, S., and Stillinger, F. H.: Computer generation of dense polydisperse sphere packings, J. Chem. Phys., 117, 8212–8218, 2002.
Kohn, M. J. and Northrup, C. J.: Taking mylonite temperatures, The Geological society of America, 37, 47–50, 2009.
Labrousse, L., Prouteau, G., and Ganzhorn, A.-C.: Continental exhumation triggered by partial melting at ultrahigh pressure, Geology, 39, 1171–1174, 2011.
MacRae, N. D. and Nesbitt, H. W.: Partial melting of common metasedimantary rocks: an mass balance approach, Contrib. Mineral. Petr., 75, 21–26, 1980.
McNamara, D. E., Owens, T. J., and Walter, W. R.: Propagation characteristics of Lg across the Tibetan plateau, B. Seismol. Soc. Am., 86, 457–469, 1996.

SED
6, 1299–1333, 2014

Merlet, C.: An accurate computer correction program for quantitative electron probe microanalysis, Mikrochim. Acta, 114/115, 363–376, 1994.
Merlet, C. and Bodinier, J. L.: Electron microprobe determination of minor and trace transition elements in silicate mineral: a method and its application to mineral zoning in the peridotite nodule phn 1611, Chem. Geol., 83, 55–69, 1990.
Mondou, M., Egydio-Silva, M., Vauchez, A., Raposo, M. I. B., Bruguier, O., and Oliveira, A. F.: Complex, 3-D strain patterns in a synkinematic tonalite batholith from the Araçuaí Neoproterozoic orogen (Eastern Brazil): evidence from combined magnetic and isotopic chronology studies, J. Struct. Geol., 39, 158–179, doi:10.1016/j.jsg.2012.02.015, 2012.
Munhá, J. M. U., Cordani, U. G., Tassinari, C. C. G., and Palacios, T.: Petrologia e termocronologia de gnaisses migmatíticos da faixa de dobramentos araçuaí (espirito santo, brasil), Revista Brasileira de Geociências, 35, 123–134, 2005.
Negrini, M., Stunitz, H., Berger, A., and Morales, L. F. G.: The effect of deformation on the TitaniQ geothermobarometers: an experimental study, Contrib. Mineral. Petr., 167, 982, doi:0.1007/s00410-014-0982-x., 2014.
Nelson, K. D., Zhao, W., Brown, L. D., Kuo, J., Che, J., Liu, X., Klemperer, S. L., Makovsky, Y., Meissner, R., Mechie, J., Kind, R., Wenzel, F., Ni, J., Nabelek, J., Chen, L., Tan, H., Wei, W., Jones, A. G., Booker, J., Unsworth, M., Kidd, W. S. F., Hauck, M., Alsdorf, D., Ross, A., Cogan, M., Wu, C., Sandvol, E. A., and Edwards, M.: Partially molten middle crust beneath southern Tibet; synthesis of Project INDEPTH results, Science, 274, 1684–1688, 1996.
Oliveira, M.-J. R., Pinto, C. P., Féboli, W. L., and Alves dos Santos, R.: Projeto Leste – Relatorio mapa integrado 1 : 500 000 – Geologia estrutural e tectônica, CPRM – COMIG, Belo Horizonte, 2000.
Pedrosa-Soares, A. C., Queiroga, G. N., Gradim, C. T., Roncato, J. G., Novo, T. A., Jacobsohn, T., and Silva, K. L.: Programa Geologia do Brasil, Mapeamento geológico e nota explicativa da Folha Mantena (SE-24-Y-a-vi), escala 1 : 100 000, Contrato CPRM 059/PR/05-UFMG (iGC/CPMC), CD-ROM, 2006.
Petitgirard, S., Vauchez, A., Egydio-Silva, M., Bruguier, O., Camps, P., Monié, P., Babinski, M., and Mondou, M.: Conflicting structural and geochronological data from the Ibituruna quartz-syenite (SE Brazil): effect of protracted orogeny and slow cooling rate? in: Hot Orogens Special Issue Tectonophysics, edited by: Chardon, D. and Rey, P., 477, 174–196, 2009.
Roscoe, R.: The viscosity of suspensions of rigid spheres, Brit. J. Appl. Phys., 13, 267–269, 1952.

SED
6, 1299–1333, 2014

Rosenberg, C. L. and Handy, M. R.: Experimental deformation of partially melted granite revisited: implications for the continental crust, J. Metamorph. Geol., 23, 19–28, 2005.
Sawyer, E. W.: Working with migmatites, Mineralogical Association of Canada short course 38, 158 pp., 2008.
Scaillet, B., Holtz, F., Whittington, A., and Pichavant, M.: Phase equilibrium constraints on the viscosity of silicic magmas, 1. Volcanic-plutonic comparison, J. Geophys. Res., 103, 27257–27266, 1998.
Schmitt, R. S., Trouw, R. A. J., Van Schmus, W. R., and Pimentel, M. M.: Late amalgamation in the central part of West Gondwana: new geochronological data and the characterization of a Cambrian collisional orogeny in the Ribeira Belt (SE Brazil), Precambrian Res., 133, 29–61, 2004.
Storm, L. C. and Spear, F. S.: Application of the titanium- in-quartz thermometer to pelitic migmatites from the Adirondack Highlands, New York, J. Metamorph. Geol., 27, 479–494, 2009.
Trompette, R.: Geology of Western Gondwana (2000–500 Ma), Balkema, Rotterdam, 350 pp., 1994.
Unsworth, M. J., Jones, A. G., Wei, W., Marquis, G., Gokarn, S. G., and Spratt, J. E. (INDEPTH-MT TEAM): Crustal rheology of the Himalaya and Southern Tibet inferred from magnetotelluric data, Nature, 438, 78–81, 2005.
Vauchez, A., Egydio-Silva, M., Babinski, M., Tommasi, A., Uhlein, A., and Liu, D.: Deformation of a pervasively molten middle crust: insights from the Neoproterozoic Ribeira-Araçuaí orogen (SE Brazil). Terra Nova, 19, 278–286, 2007.
Wark, D. A. and Watson, E. B.: TitaniQ: a titanium-in- quartz geothermometer, Contrib. Mineral. Petr., 152, 743–754, 2006.
White, R. W., Powell, R., and Clarke, G. L.: Prograde Metamorphic Assemblage Evolution during Partial Melting of Metasedimentary Rocks at Low Pressures: Migmatites from? Mt Stafford, Central Australia, J. Petrol., 44, 1937–1960, 2003.
Wu, C. M., Zhang, J. Z., and Ren, L. D.: Empirical Garnet–Biotite–Plagioclase–Quartz (GBPQ) geobarometry in medium- to high-grade metapelites, J. Petrol., 45, 1907–1921, 2004.

SED
6, 1299–1333, 2014

Table 1. Titanium content and calculated TitaniQ temperatures for each analytical spot, with the average values shown for each sample.

Sample-crystal number Migmatitic granulite	Ti (ppm)	Temperature (°C)	Sample-crystal number Metatexite	Ti (ppm)	Temperature (°C)
ar1296pt01	92	737	ar1326pt02	112	761
ar1296pt01	98	745	ar1326pt02	157	804
ar1296pt01	89	733	ar1326pt02	157	804
ar1296pt01	27	611	ar1326pt02	155	803
ar1296pt01	83	725	ar1326pt02	154	802
ar1296pt02	112	761	ar1326pt02	103	751
ar1296pt02	110	759	ar1326pt02	15	561
ar1296pt02	109	758	ar1326pt02	157	804
ar1296pt02	118	767	ar1326pt02	150	798
ar1296pt02	136	785	ar1326pt02	138	787
ar1296pt02	141	790	ar1326pt02	137	786
ar1296pt03	91	736	ar1326pt03	158	805
ar1296pt03	107	755	ar1326pt03	152	800
ar1296pt03	156	804	ar1326pt03	145	794
ar1296pt03	265	879	ar1326pt03	156	804
ar1296pt03	103	751	ar1326pt03	143	792
ar1296pt04	97	744	ar1326pt03	129	779
ar1296pt04	91	736	ar1326pt03	124	774
ar1296pt04	101	748	ar1326pt03	110	759
ar1296pt04	122	772	ar1326pt03	127	777
ar1296pt04	103	751	ar1326pt03	128	778
ar1296pt04	88	732	ar1326pt03	137	786
ar1296pt05	104	752	ar1326pt03	148	797
ar1296pt05	112	761	ar1326pt03	157	804
ar1296pt05	125	775	ar1326pt03	136	785
ar1296pt05	124	774	ar1326pt03	131	781
ar1296	112	755 ± 16	ar1326pt03	123	773
Diatexite			ar1326pt03	135	785
ar1299pt01	117	766	ar1326pt03	128	778
ar1299pt01	142	791	ar1326pt06	131	781
ar1299pt01	136	785	ar1326pt06	152	800
ar1299pt01	123	773	ar1326pt06	148	797
ar1299pt01	128	778	ar1326pt06	144	793
ar1299pt01	126	776	ar1326pt06	144	793
ar1299pt01	132	782	ar1326pt06	146	795
ar1299pt01	153	801	ar1326pt06	157	804
ar1299pt01	136	785	ar1326pt06	162	809
ar1299pt01	120	770	ar1326pt06	160	807
ar1299pt01	132	782	ar1326pt06	154	802
ar1299pt01	130	780	ar1326pt06	160	807
ar1299pt01	124	774	ar1326pt06	157	804
ar1299pt01	130	780	ar1326pt06	145	794
ar1299pt01	119	769	ar1326pt06	145	794
ar1299pt01	132	782	ar1326pt06	140	789
ar1299pt01	115	764	ar1326pt06	123	773
ar1299pt01	114	763	ar1326pt06	151	799
ar1299pt03	117	766	ar1326pt06	152	800
ar1299pt03	125	775	ar1326pt06	154	802
ar1299pt03	118	767	ar1326pt06	148	797
ar1299pt03	118	767	ar1326pt06	142	791
ar1299pt03	132	782	ar1326pt06	156	804
ar1299pt03	127	777	ar1326pt06	147	796
ar1299pt03	149	797	ar1326pt06	124	774
ar1299pt03	140	789	ar1326pt07	153	801

SED
6, 1299–1333, 2014

Table 1. Continued.

Sample-crystal number Migmatitic granulite	Ti (ppm)	Temperature (°C)	Sample-crystal number Metatexite	Ti (ppm)	Temperature (°C)
ar1299pt03	136	785	ar1326pt07	160	807
ar1299pt03	124	774	ar1326pt07	160	807
ar1299pt03	138	787	ar1326pt07	154	802
ar1299pt03	108	757	ar1326pt07	166	812
ar1299pt03	122	772	ar1326pt07	162	809
ar1299pt03	144	793	ar1326pt07	170	815
ar1299pt03	135	785	ar1326pt07	171	816
ar1299pt03	138	787	ar1326pt07	165	811
ar1299pt03	123	773	ar1326pt07	161	808
ar1299pt04	122	772	ar1326pt07	150	798
ar1299pt04	119	769	ar1326pt07	159	806
ar1299pt04	107	755	ar1326pt07	160	807
ar1299pt04	139	788	ar1326pt07	162	809
ar1299pt04	139	788	ar1326pt07	161	808
ar1299pt04	147	796	ar1326	145	792 ± 17
ar1299pt04	162	809	Migmatitic kinzigites		
ar1299pt04	141	790	ar1083pt01	139	788
ar1299pt04	156	804	ar1083pt01	145	794
ar1299pt04	135	785	ar1083pt01	150	798
ar1299pt04	150	798	ar1083pt01	153	801
ar1299pt04	136	785	ar1083pt01	152	800
ar1299pt04	134	784	ar1083pt01	152	800
ar1299pt04	134	784	ar1083pt01	145	794
ar1299pt04	112	761	ar1083pt03	134	784
ar1299pt04	122	772	ar1083pt03	136	785
ar1299pt04	143	792	ar1083pt03	144	793
ar1299pt04	146	795	ar1083pt03	135	785
ar1299pt04	144	793	ar1083pt03	134	784
ar1299pt04	152	800	ar1083pt03	136	785
ar1299pt04	141	790	ar1083pt04	126	776
ar1299pt05	123	773	ar1083pt04	142	791
ar1299pt05	115	764	ar1083pt04	144	793
ar1299pt05	124	774	ar1083pt04	144	793
ar1299pt05	127	777	ar1083pt04	138	787
ar1299pt05	124	774	ar1083pt04	134	784
ar1299pt05	130	780	ar1083pt04	127	777
ar1299pt05	121	771	ar1083pt04	127	777
ar1299pt05	126	776	ar1083pt04	134	784
ar1299pt05	140	789	ar1083pt04	148	797
ar1299pt05	118	767	ar1083pt04	127	777
ar1299pt05	109	758	ar1083pt04	112	761
ar1299	130	780 ± 16	ar1083	138	787 ± 17
ar1258pt01	82	724	ar949pt01	154	802
ar1258pt01	102	750	ar949pt01	167	813
ar1258pt01	79	720	ar949pt01	167	813
ar1258pt01	75	714	ar949pt01	170	815
ar1258pt01	82	724	ar949pt01	171	816
ar1258pt01	88	732	ar949pt01	175	819
ar1258pt01	85	728	ar949pt01	175	819
ar1258pt01	143	792	ar949pt01	161	808
ar1258pt01	92	737	ar949pt01	156	804
ar1258pt01	112	761	ar949pt01	155	803
ar1258pt01	93	739	ar949pt01	133	783
ar1258pt01	88	732	ar949pt01	152	800
ar1258pt01	92	737	ar949pt01	159	806

SED
6, 1299–1333, 2014

Table 1. Continued.

Sample-crystal number Migmatitic granulite	Ti (ppm)	Temperature (°C)	Sample-crystal number Metatexite	Ti (ppm)	Temperature (°C)
ar1258pt01	96	742	ar949pt01	168	814
ar1258pt01	87	731	ar949pt01	181	824
ar1258pt01	126	776	ar949pt01	179	822
ar1258pt01	85	728	ar949pt01	163	809
ar1258pt01	101	748	ar949pt01	169	814
ar1258pt01	99	746	ar949pt01	156	804
ar1258pt01	86	729	ar949pt01	147	796
ar1258pt01	88	732	ar949pt02	140	789
ar1258pt01	86	729	ar949pt02	139	788
ar1258pt01	82	724	ar949pt02	109	758
ar1258pt01	78	718	ar949pt02	114	763
ar1258pt01	77	717	ar949pt02	133	783
ar1258pt01	83	725	ar949pt03	107	755
ar1258pt01	103	751	ar949pt03	126	776
ar1258pt02	97	744	ar949pt03	125	775
ar1258pt02	104	752	ar949pt03	122	772
ar1258pt02	88	732	ar949pt03	132	782
ar1258pt02	99	746	ar949pt03	111	760
ar1258pt02	112	761	ar949pt03	111	760
ar1258pt03	89	733	ar949pt03	127	777
ar1258pt03	97	744	ar949pt03	108	757
ar1258pt03	147	796	ar949pt03	130	780
ar1258pt03	101	748	ar949pt03	134	784
ar1258pt03	77	717	ar949pt03	118	767
ar1258pt03	87	731	ar949pt04	137	786
ar1258pt03	108	757	ar949pt04	151	799
ar1258pt03	89	733	ar949pt04	156	804
ar1258pt03	99	746	ar949pt04	151	799
ar1258pt03	121	771	ar949pt04	152	800
ar1258pt03	84	727	ar949pt04	146	795
ar1258pt03	100	747	ar949pt04	145	794
ar1258pt03	93	739	ar949pt04	144	793
ar1258pt04	96	742	ar949pt04	159	806
ar1258pt04	97	744	ar949pt04	151	799
ar1258pt04	96	742	ar949pt04	144	793
ar1258pt04	88	732	ar949pt04	158	805
ar1258pt04	90	735	ar949pt04	160	807
ar1258pt04	89	733	ar949pt04	152	800
ar1258pt04	91	736	ar949pt04	158	805
ar1258pt04	108	757	ar949pt04	155	803
ar1258pt04	95	741	ar949pt04	153	801
ar1258pt04	101	748	ar949pt04	158	805
ar1258pt04	97	744	ar949pt04	155	803
ar1258pt04	112	761	ar949pt04	130	780
ar1258pt04	102	750	ar949	147	794 ± 17

SED
6, 1299–1333, 2014

Table 1. Continued.

Sample-crystal number Migmatitic granulite	Ti (ppm)	Temperature (°C)	Sample-crystal number Metatexite	Ti (ppm)	Temperature (°C)
ar1258pt05	131	781			
ar1258pt05	98	745			
ar1258pt05	91	736			
ar1258pt05	92	737			
ar1258pt05	102	750			
ar1258pt05	94	740			
ar1258pt05	103	751			
ar1258pt05	111	760			
ar1258pt05	120	770			
ar1258pt05	181	824			
ar1258pt05	92	737			
ar1258pt05	93	739			
ar1258pt05	202	839			
ar1258pt05	100	747			
ar1258pt05	116	765			
ar1258pt05	99	746			
ar1258pt05	97	744			
ar1258pt05	137	786			
ar1258pt05	101	748			
ar1258pt05	98	745			
ar1258pt05	123	773			
ar1258pt05	106	754			
ar1258pt05	108	757			
ar1258pt05	95	741			
ar1258pt05	109	758			
ar1258pt05	129	779			
ar1258pt05	100	747			
ar1258pt05	85	728			
ar1258	101	747 ± 15			

SED
6, 1299–1333, 2014

Table 2. Summarized geothermobarometric results for the studied rocks.

Identification	Analysis	Thermometer	T (°C)	Reference	Barometer	P (MPa)
Ar949	Core	grt-bt	802-832	Ferry and Spear (1978)	GPBQ	
	Rim	grt-bt	607-742	Ferry and Spear (1978)	GPBQ	349–447
	Core	grt-crd	797-824	Bhattacharya et al. (1988)	GPBQ	
	Rim	grt-crd	756-789	Bhattacharya et al. (1988)	GPBQ	
Ar1083	Core	grt-bt	826-842	Ferry and Spear (1978)	GPBQ	296–338
	Rim	grt-bt	633-679	Ferry and Spear (1978)	GPBQ	321–335
Ar1076c	Core	grt-bt	765-835	Ferry and Spear (1978)	GPBQ	704
Ar1076d	Core	grt-bt	721-814	Ferry and Spear (1978)	GPBQ	
	Rim	grt-bt	558-668	Ferry and Spear (1978)	GPBQ	
	Core	grt-opx	792-831	Bhattacharya et. al. (1991)	GPBQ	559–612
	Rim	grt-opx	652-784	Bhattacharya et. al. (1991)	GPBQ	651–652

SED
6, 1299–1333, 2014

Table 3. Summarized oxide mineral chemistry for the studied rocks, including the major element composition (wt %) of selected garnet, biotite, plagioclase, orthopyroxene and cordierite.

Phase	SiO_2	Al_2O_3	TiO_2	Na_2O	MgO	FeO	K_2O	CaO	Cr_2O_3	MnO	NiO	Total
garnet	39.0	21.8	0.0	0.0	7.0	32.0	0.0	1.2	0.0	0.8	0.0	101.8
	38.7	21.8	0.0	0.0	7.3	31.5	0.0	1.2	0.0	0.8	0.0	101.4
	38.6	21.9	0.0	0.0	7.7	31.0	0.0	1.2	0.0	0.8	0.0	101.3
	38.7	21.9	0.0	0.0	7.9	31.0	0.0	1.2	0.0	0.8	0.0	101.6
	38.8	22.0	0.0	0.0	7.8	31.3	0.0	1.2	0.0	0.7	0.0	101.9
	38.5	21.9	0.0	0.0	7.7	31.1	0.0	1.2	0.0	0.8	0.0	101.2
	38.5	21.9	0.0	0.0	8.2	30.3	0.0	1.2	0.0	0.7	0.0	100.9
	38.6	22.0	0.0	0.0	8.1	30.6	0.0	1.2	0.0	0.7	0.0	101.4
biotite	36.4	16.4	5.8	0.1	11.6	15.6	9.9	0.0	0.1	0.0	0.0	95.9
	36.4	16.2	6.1	0.2	13.7	12.6	10.0	0.0	0.1	0.0	0.0	95.2
	36.9	17.4	6.1	0.4	13.3	12.4	9.4	0.0	0.1	0.0	0.0	96.2
	37.1	17.2	5.1	0.2	13.9	12.5	9.9	0.0	0.1	0.0	0.0	96.0
	37.2	16.9	5.9	0.2	14.5	11.0	10.0	0.0	0.1	0.0	0.0	95.9
	36.5	17.3	5.3	0.3	12.8	12.4	9.3	0.0	0.1	0.0	0.0	94.1
	36.3	17.2	6.3	0.3	12.0	13.9	9.6	0.0	0.1	0.0	0.0	95.8
cordierite	49.3	33.0	0.0	0.1	9.3	6.5	0.0	0.0	0.0	0.1	0.0	98.3
	49.4	33.4	0.0	0.1	9.7	6.4	0.0	0.0	0.0	0.1	0.0	99.1
	49.1	33.0	0.0	0.1	9.3	6.8	0.0	0.0	0.0	0.1	0.0	98.3
	49.3	33.1	0.0	0.1	9.3	6.7	0.0	0.0	0.0	0.1	0.0	98.6
	49.1	33.1	0.0	0.1	9.2	6.8	0.0	0.0	0.0	0.1	0.0	98.5
Plagioclase	59.8	24.9	0.0	7.8	0.0	0.0	0.3	6.7	0.0	0.0	0.0	99.5
	60.0	25.1	0.0	7.7	0.0	0.0	0.3	6.9	0.0	0.0	0.0	100.0
	60.1	24.9	0.0	7.7	0.0	0.0	0.3	6.7	0.0	0.0	0.0	99.9
							Ar1083					
garnet	38.6	21.8	0.0	0.0	7.1	32.1	0.0	0.9	0.0	1.1	0.0	101.8
	38.7	22.0	0.0	0.0	7.1	31.5	0.0	0.9	0.0	1.1	0.0	101.4
	38.7	21.8	0.0	0.0	7.2	31.7	0.0	0.9	0.0	1.1	0.0	101.5
	39.3	22.1	0.0	0.0	7.1	31.7	0.0	0.9	0.0	0.0	0.0	102.3
	38.5	21.9	0.0	0.0	7.1	31.8	0.0	0.9	0.0	1.1	0.0	101.4
Biotite	35.6	17.3	6.3	0.4	13.4	12.2	9.6	0.0	0.1	0.0	0.0	94.8
	36.6	17.3	6.5	0.3	13.2	12.6	9.7	0.0	0.1	0.0	0.0	96.3
	36.9	17.4	6.4	0.3	12.8	12.7	9.8	0.0	0.1	0.0	0.0	96.4
	36.8	17.0	5.5	0.2	11.1	15.9	9.9	0.0	0.1	0.0	0.0	96.5
	36.9	16.7	5.5	0.1	11.3	15.5	10.0	0.0	0.1	0.0	0.0	96.2
plagioclase	61.6	24.2	0.0	8.3	0.0	0.0	0.2	5.7	0.0	0.0	0.0	100.1
	62.3	23.8	0.0	8.5	0.0	0.0	0.3	5.2	0.0	0.0	0.0	100.2
	61.7	24.2	0.0	8.4	0.0	0.0	0.2	5.6	0.0	0.0	0.0	100.3
	61.2	24.3	0.0	8.5	0.0	0.1	0.2	5.9	0.0	0.0	0.0	100.2
	61.6	24.4	0.0	8.4	0.0	0.0	0.2	5.8	0.0	0.0	0.0	100.4

SED
6, 1299–1333, 2014

Table 3. Continued.

Phase	SiO_2	Al_2O_3	TiO_2	Na_2O	MgO	FeO	K_2O Ar949	CaO	Cr_2O_3	MnO	NiO	Total
							Ar1076c					
garnet	38.3	21.7	0.0	0.0	5.8	32.4	0.0	2.1	0.0	1.3	0.0	101.8
	38.3	21.6	0.0	0.0	5.3	33.2	0.0	1.8	0.0	1.4	0.0	101.7
biotite	36.2	16.2	4.8	0.1	10.5	18.2	9.8	0.0	0.1	0.1	0.0	96.0
	36.3	16.1	4.9	0.2	10.6	18.2	9.8	0.0	0.1	0.0	0.0	96.2
	36.3	16.4	4.8	0.2	11.4	17.2	9.8	0.0	0.1	0.0	0.0	96.1
	36.4	16.2	4.9	0.1	10.5	18.2	9.6	0.0	0.0	0.0	0.0	96.0
Plagioclase	60.0	25.4	0.0	7.6	0.0	0.1	0.2	7.1	0.0	0.0	0.0	100.4
							Ar1076d					
garnet	37.9	21.4	0.0	0.0	5.7	32.4	0.0	2.1	0.0	1.3	0.0	100.8
	37.8	21.5	0.0	0.0	4.4	34.7	0.0	1.7	0.1	1.4	0.0	101.5
	37.9	21.6	0.0	0.0	6.0	31.6	0.0	2.2	0.0	1.3	0.0	100.7
	38.4	21.7	0.0	0.0	6.3	31.6	0.0	2.1	0.0	1.2	0.0	101.3
	37.5	21.3	0.0	0.0	5.1	33.5	0.0	1.8	0.0	1.3	0.0	100.6
	37.4	21.0	0.0	0.0	5.1	33.9	0.0	1.3	0.0	1.4	0.0	100.1
	37.6	21.3	0.0	0.0	5.3	33.1	0.0	1.7	0.0	1.4	0.0	100.3
	40.0	22.6	0.0	0.0	5.4	32.1	0.0	1.8	0.0	1.3	0.0	103.2
	38.4	21.6	0.0	0.0	6.1	31.3	0.0	1.9	0.0	1.2	0.0	100.7
	38.4	21.6	0.0	0.0	6.2	31.8	0.0	2.0	0.0	1.3	0.0	101.2
	38.3	21.6	0.0	0.0	6.3	31.9	0.0	1.9	0.0	1.3	0.0	101.3
	38.2	21.7	0.0	0.0	6.3	32.0	0.0	1.8	0.0	1.3	0.0	101.2
	38.3	21.4	0.0	0.0	6.2	31.3	0.0	1.8	0.0	1.3	0.0	100.3
	38.4	21.7	0.0	0.0	6.2	31.9	0.0	1.8	0.0	1.3	0.0	101.3
biotite	36.0	16.2	4.7	0.1	11.1	17.6	9.8	0.0	0.1	0.0	0.0	95.7
	35.8	16.2	4.6	0.2	11.1	17.8	9.6	0.0	0.1	0.0	0.0	95.3
	36.3	16.2	4.6	0.1	11.7	17.3	9.9	0.0	0.1	0.0	0.0	96.1
	36.2	16.2	4.6	0.1	11.6	17.4	9.8	0.1	0.1	0.0	0.0	96.1
	36.3	16.2	4.6	0.2	13.4	14.3	9.7	0.0	0.1	0.0	0.0	94.8
	36.4	16.1	4.5	0.2	11.6	16.8	9.8	0.0	0.1	0.0	0.0	95.6
	36.2	16.1	4.5	0.1	11.4	17.7	9.8	0.0	0.0	0.0	0.0	96.0
	36.3	16.2	4.3	0.1	11.4	17.3	9.7	0.0	0.1	0.0	0.0	95.6
	36.4	16.2	4.3	0.1	11.3	17.0	9.8	0.0	0.1	0.0	0.0	95.3
	35.9	16.2	4.4	0.1	11.5	17.2	9.7	0.0	0.1	0.0	0.0	95.2
	36.3	16.3	4.4	0.1	11.3	17.3	9.8	0.0	0.1	0.0	0.0	95.6
	36.3	16.2	4.5	0.1	11.4	17.0	9.7	0.0	0.1	0.0	0.0	95.3
	35.9	16.1	4.3	0.1	11.6	17.5	9.8	0.0	0.1	0.0	0.0	95.5
opx	49.3	2.9	0.1	0.0	15.6	31.0	0.0	0.1	0.0	0.5	0.0	99.5
	49.0	2.9	0.1	0.0	15.8	30.9	0.0	0.2	0.0	0.5	0.0	99.3
	49.7	2.8	0.1	0.0	15.9	30.6	0.0	0.1	0.0	0.4	0.0	99.7
	49.3	3.0	0.1	0.0	15.7	31.2	0.0	0.1	0.0	0.5	0.0	99.9
Plagioclase	59.4	25.0	0.0	7.6	0.0	0.1	0.3	6.7	0.0	0.0	0.0	99.1
	59.9	24.9	0.0	7.5	0.0	0.1	0.1	6.4	0.0	0.0	0.0	98.9
	59.4	24.9	0.0	7.7	0.0	0.0	0.3	6.7	0.0	0.0	0.0	99.1
	59.2	24.8	0.0	7.5	0.0	0.0	0.3	6.7	0.0	0.0	0.0	98.5

SED
6, 1299–1333, 2014

Table 4. Bulk rock composition of the leucosomes of representative anatectic rocks.

Wt%	Ar1113	Ar952	Ar1171	Ar1172	Ar1178	Ar1184	Ar1185
SiO_2	72.53	72.43	71.61	72.81	71.45	69.73	71.18
Al_2O_3	13.78	14.59	14.31	13.89	14.29	15.11	14.59
Fe_2O_3	2.65	1.62	2.94	2.26	2.95	3.11	2.81
MgO	0.74	0.45	0.68	0.53	0.75	0.90	0.69
CaO	2.00	0.76	1.37	1.46	1.81	2.51	1.67
Na_2O	2.42	2.57	2.46	2.55	2.52	2.85	2.73
K_2O	4.37	5.92	5.50	5.30	4.83	4.11	4.90
TiO_2	0.40	0.33	0.38	0.32	0.43	0.52	0.38
P_2O_5	0.19	0.28	0.12	0.19	0.21	0.21	0.24
MnO	0.05	0.01	0.04	0.03	0.05	0.05	0.04
LOI	0.8	0.9	0.5	0.6	0.6	0.8	0.7
Sum	99.89	99.86	99.92	99.93	99.89	99.86	99.90

SED
6, 1299–1333, 2014

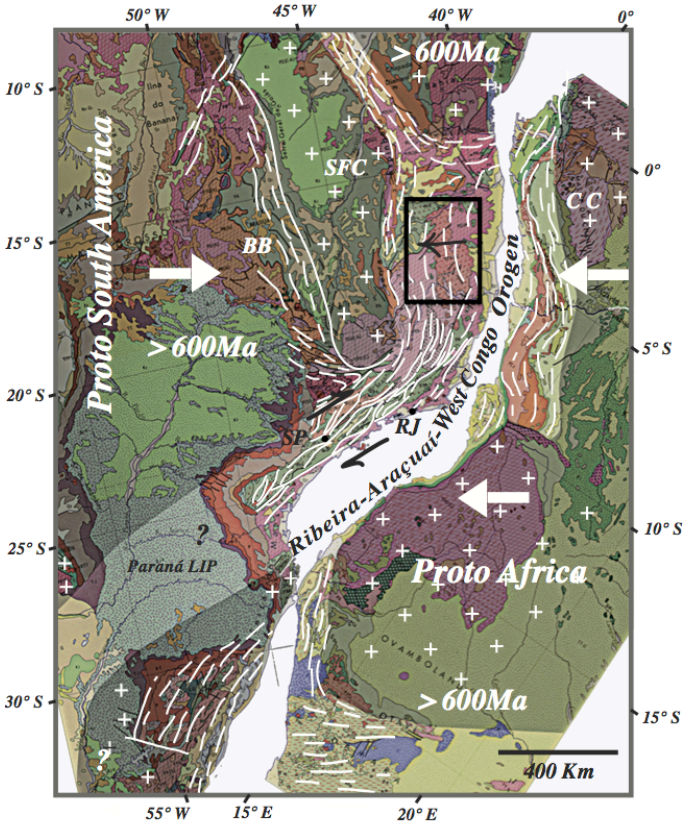

Figure 1. Schematic reconstitution of the position of South America and Africa before the opening of the South Atlantic (Vauchez et al., 2007). Shaded areas represent domains where collision occurred before ~ 600 Ma (white crosses = cratonic domains; white lines = Neoproterozoic belts). The area delimited by the rectangle represents the location of Fig. 2. Arrows show the convergence between South America and Africa. Small black arrows show the main kinematics. CC = Congo craton, BB = Brasilia belt, SP = São Paulo, RJ = Rio de Janeiro.

SED
6, 1299–1333, 2014

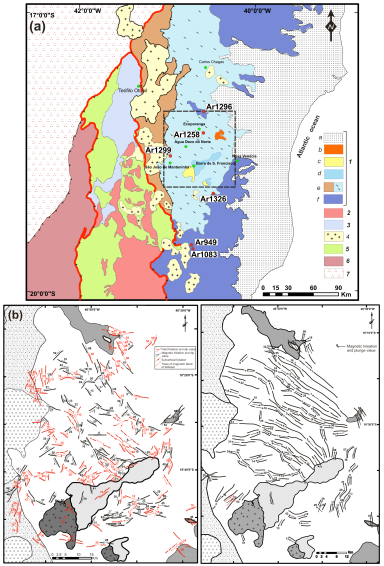

Figure 2. (a) Simplified geological map (after Oliveira et al., 2000; Vauchez et al., 2007) showing the main domains of the Araçuaí belt and the location of the samples selected for this study: the eastern domain (1) comprises a thick (> 10 km) layer of diatexites, metatexites and anatectic granites **(e)** associated with migmatitic granulites **(f)** and intruded by granite **(c)** and charnockite **(d)**. **(a)** and **(b)** represent the Phanerozoic cover. The central domain comprises a syn-collisional magmatic complex (2 = Galiléia batholith; 3 = São Vitor tonalite) intruded in HT metasediments (5). The western domain involves HT metasedimentary mylonites injected by abundant synkinematic leucocratic magma (6) thrust upon the para-autochthonous metasedimentary cover of the São Francisco craton (7). Late orogenic (~ 520 My, Mondou et al., 2012) porphyritic granitoids associated with charnockites (4) intrude the stack of allochthonous units. The red line represents the boundary between lithological domains. The green pentagons represent cities. The dashed box shows the location of Fig. 2b (foliation and lineation maps of the anatectic domain from Cavalcante et al., 2013).

SED
6, 1299–1333, 2014

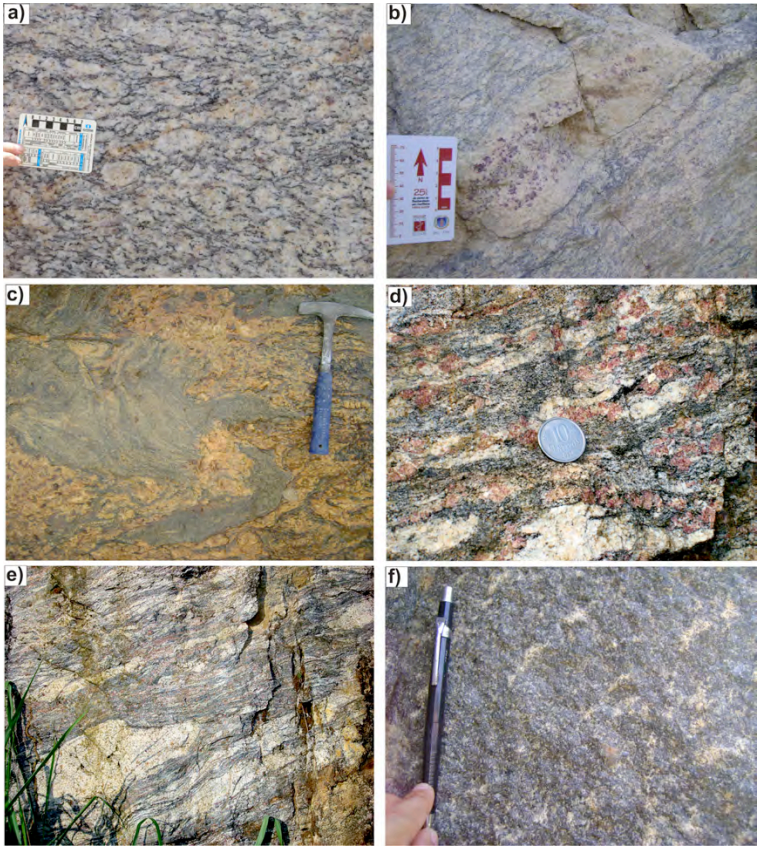

Figure 3. Pictures of outcrops representative of the studied rocks: **(a)** an example of diatexite with well-marked magmatic foliation characterized by preferred alignment of biotite and feldspar; **(b)** diatexite with leucosome rich in garnet and feldspar; **(c)** diatexite displaying scholle feature; **(d)** and **(e)** migmatitic kinzigites displaying stromatic leucosomes embedded between gneissic foliations; **(f)** a migmatitic granulite with small pockets of melt.

SED
6, 1299–1333, 2014

Figure 4. Pictures (left) and schematic drawing (right) of partially molten kinzigites of the Araçuaí belt. White represents the in situ leucosomes and gray represents the residuum and/or paleosome portions.

SED
6, 1299–1333, 2014

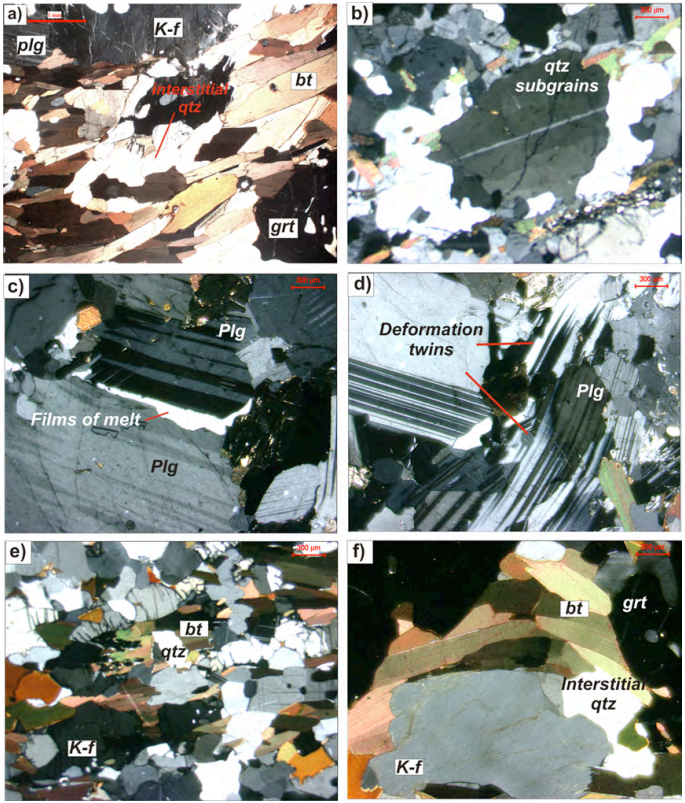

Figure 5. Photomicrographs of anatexites and migmatitic granulites. **(a)** Large interstitial quartz and preferred orientation of biotite characterizing the magmatic foliation, **(b)** quartz subgrains representing the record of the intracrystalline deformation, **(c)** film of quartz crystallized along grains boundaries that likely represent former films of melt, **(d)** deformation twins in plagioclase feldspar, **(e)** preferred orientation of biotite grains, and **(f)** large K-feldspar grains associated with interstitial quartz and arched biotite.

SED
6, 1299–1333, 2014

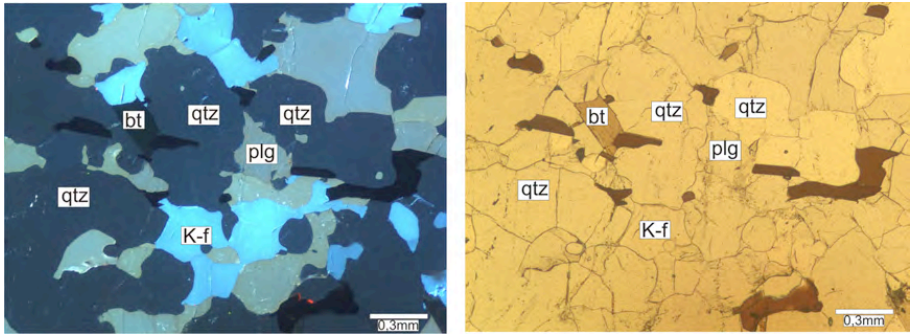

Figure 6. CL (right) and true-color (left) images of the migmatitic kinzigite (sample Ar949) displaying the intense homogenous dark blue of quartz grains.

SED
6, 1299–1333, 2014

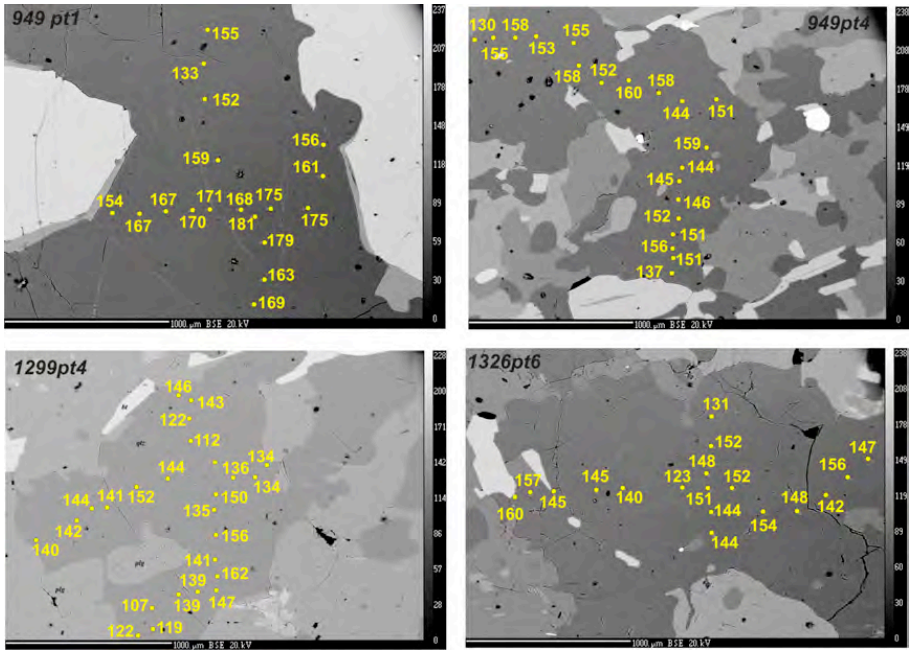

Figure 7. Spots along transverse profiles and respective titanium concentrations (ppm) in quartz from migmatitic kinzigite (samples Ar949 and Ar1326) and from diatexite (Ar1299).

SED
6, 1299–1333, 2014

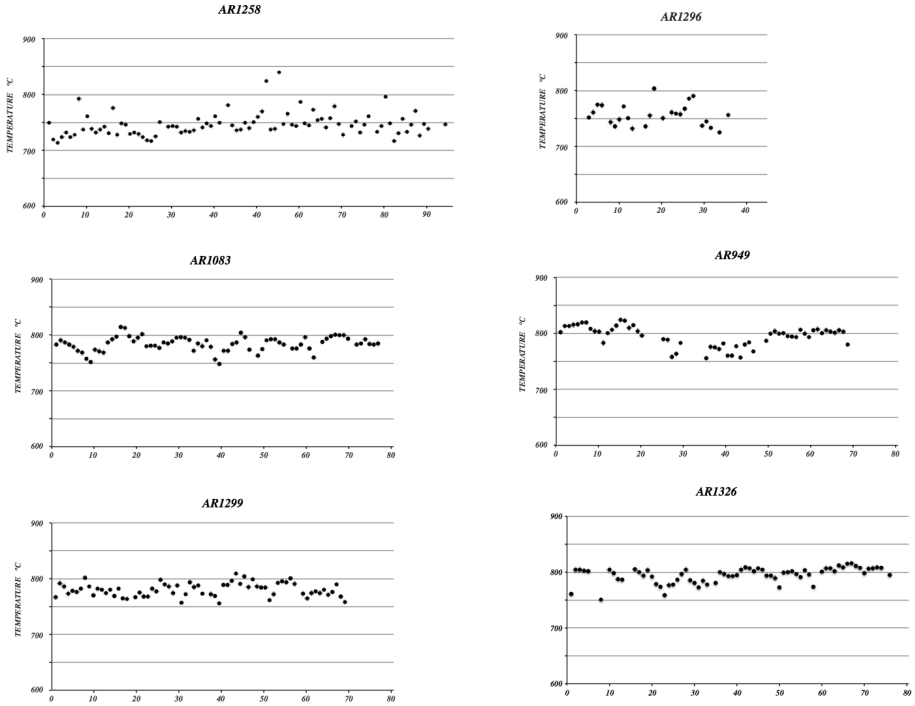

Figure 8. Calculated temperature (y-axis) for each individual Ti-in-quartz analysis (x-axis = analysis number in Table 1.

SED
6, 1299–1333, 2014